

Suzaku Observations of Tycho’s Supernova Remnant

Toru TAMAGAWA,^{1,2} Asami HAYATO,^{1,2} Satoshi NAKAMURA,^{1,2} Yukikatsu TERADA,³ Aya BAMBA,⁴ Junko S. HIRAGA,¹
John P. HUGHES,⁵ Una HWANG,⁶ Jun KATAOKA,⁷ Kenzo KINUGASA,⁸ Hideyo KUNIEDA,⁹ Takaaki TANAKA,⁴
Hiroshi TSUNEMI,¹⁰ Masaru UENO,⁷ Stephen S. HOLT,¹¹ Motohide KOKUBUN,⁴ Emi MIYATA,¹⁰
Andrew SZYMKOWIAK,¹² Tadayuki TAKAHASHI,⁴ Keisuke TAMURA,⁴ Daisuke UENO,⁹ and Kazuo MAKISHIMA^{13,1}
¹RIKEN, 2-1 Hirosawa, Wako, Saitama 351-0198

tamagawa@riken.jp

²Department of Physics, Tokyo University of Science, 1-3 Kagurazaka, Shinjyuku-ku, Tokyo 162-8601

³Department of Physics, School of Science, Saitama University, 255 Shimo-Ohkubo, Sakura, Saitama 338-8570

⁴Institute of Space and Astronautical Science, Japan Aerospace Exploration Agency, 3-1-1 Yoshinodai, Sagami-hara, Kanagawa 229-8510

⁵Department of Physics and Astronomy, Rutgers University, 136 Frelinghuysen Road, Piscataway, NJ 08854-8019, USA

⁶NASA Goddard Space Flight Center, Greenbelt, MD 20771, USA

⁷Department of Physics, Faculty of Science, Tokyo Institute of Technology, 2-12-1 Meguro-ku, Ohokayama, Tokyo 152-8551

⁸Gunma Astronomical Observatory, 6860-86 Nakayama, Takayama-mura, Agatsuma-gun, Gunma 377-0702

⁹Department of Astrophysics, Nagoya University, Furo-cho, Chikusa-ku, Nagoya 464-8063

¹⁰Department of Earth and Space Science, Graduate School of Science, Osaka University, 1-1 Machikaneyama, Toyonaka, Osaka 560-0043

¹¹F. W. Olin College of Engineering, Needham, MA 02492, USA

¹²Department of Physics, Yale University, New Haven, CT 06520, USA

¹³Department of Physics, The University of Tokyo, 7-3-1 Hongo, Bunkyo-ku, Tokyo 113-0033

(Received 2008 May 2; accepted 2008 May 19)

Abstract

Tycho’s supernova remnant was observed by the XIS and HXD instruments onboard the Suzaku satellite on 2006 June 26–29 for 92 ks. The spectrum up to 30 keV was well fitted with a two-component model, consisting of a power-law with a photon index of 2.7 and a thermal bremsstrahlung model with a temperature of 4.7 keV. The former component can alternatively be modeled as synchrotron emission from a population of relativistic electrons with an estimated roll-off energy of around 1 keV. In the XIS spectra, in addition to the prominent Fe K α line (6.445 keV), we observed for the first time significant K α line emission from trace species Cr and Mn at energies of 5.48 keV and 5.95 keV, respectively. Faint K β lines from Ca (4.56 keV) and Fe (7.11 keV) were also seen. The ionization states of Cr and Mn, based on their line centroids, are estimated to be similar to that of Fe K α (Fe XV or XVI).

Key words: acceleration of particles — ISM: supernova remnants — X-rays: individual (Tycho)

1. Introduction

Extensive studies at X-ray and TeV energies have been carried out in recent years to reveal the origin of Galactic cosmic rays (CRs). Diffusive shock acceleration at the blast waves of supernova remnants (SNRs) is widely believed to be a prime source for producing CRs up to energies of the so-called “knee” in the CR spectrum around 1000 TeV. The ASCA observation of SN 1006 (Koyama et al. 1995) revealed a featureless power-law component, interpreted as originating from synchrotron emission near the outer shell and appearing well separated from a thermal component filling the projected interior. Such a clear situation is, however, not usually the case with the other youngest SNRs, in which any nonthermal synchrotron X-ray emission from the blast wave is difficult to separate from the relatively more dominant thermal X-ray components. To more readily achieve this separation, we focus on the higher energy X-ray band where the thermal contribution is low.

One of the brightest remnants among the Galactic historical supernovae is Tycho’s SNR (observed by Tycho Brahe in AD 1572). Synchrotron emission, like that from SN 1006,

has been expected from this remnant based on shock acceleration models (see, for example, Ammosov et al. 1994), at high enough X-ray brightness levels to offer the possibility of observationally separating the nonthermal from thermal emission. The first evidence for hard X-ray emission in Tycho’s SNR was provided by the A-2 experiment on HEAO 1 (Pravdo & Smith 1979), which measured the integrated spectrum of the entire remnant up to 25 keV. Using the 4.5–20 keV Ginga spectrum of the SNR, Fink et al. (1994) detected a power-law component with a photon index of $\alpha_p = 2.72$, in combination with a thermal bremsstrahlung continuum and an Fe K α emission line. The RXTE satellite detected the hard continuum spectrum up to 20 keV, and measured a photon index of $\alpha_p \sim 3$ (Petre et al. 1999).

Recent Chandra and XMM-Newton observations of Tycho’s SNR have provided spatially resolved spectra up to photon energies of around 10 keV. One remarkable feature of the high angular resolution data was the discovery of spectrally featureless, geometrically thin filaments encircling nearly the entire outer rim of the SNR (Hwang et al. 2002). Although the featureless nature of the spectra from the outer rim can be accommodated by either the power-law or

thermal bremsstrahlung model, various lines of evidence favor a nonthermal synchrotron origin for the emission (Warren et al. 2005). Detailed models for the X-ray spectra and morphology of these filaments (Cassam-Chenaï et al. 2007) strongly indicate that the outer-rim X-ray emission of this SNR comes via synchrotron radiation from electrons shock-accelerated up to energies of a few 10 TeV. Similar features have now been seen in other young remnants of historical supernovae (Bamba et al. 2005).

Tycho's SNR also shows intense atomic emission lines, which were studied in detail with Tenma by Tsunemi et al. (1986), who showed for the first time that the $K\alpha$ line energies of Si, S, Ar, Ca, and Fe were significantly lower than those expected under ionization equilibrium conditions, requiring that the X-ray emitting plasma be in a strongly under-ionized, and therefore nonequilibrium condition. Investigations of Tycho's thermal emission, especially its spatial variation, were also carried out by ASCA (Hwang & Gotthelf 1997), Chandra (Hwang et al. 2002), and XMM-Newton (Decourchelle et al. 2001). The most recent detailed results on the ejecta properties of Tycho's SNR come from Badenes et al. (2006), who compared the integrated X-ray spectrum to theoretical models for the ejecta X-ray emission of thermonuclear (i.e., Type Ia) supernovae.

In the present paper, we consider the recent broad-band X-ray observations of Tycho's SNR by the Suzaku satellite. Utilizing the long-exposure duration and the excellent CCD spectral resolution, we conducted a sensitive search for faint emission lines. We also used the broad spectral coverage of Suzaku (the remnant is detected from photon energies of 0.5 keV up to a few tens of keV) to separate the nonthermal component from the dominant thermal X-ray component.

2. Observations and Data Reduction

2.1. Observations

Launched on 2005 July 10 as a joint Japan-US mission (Mitsuda et al. 2007), Suzaku carries four X-ray telescopes (XRT: Serlemitsos et al. 2007) each of which illuminates an X-ray imaging spectrometer (XIS: Koyama et al. 2007) with a $18' \times 18'$ field of view. The payload includes a co-aligned non-imaging hard X-ray detector (HXD: Takahashi et al. 2007) as well. While the entire HXD and the high-energy portion of the XIS spectra play a major role in studying the nonthermal emission, the lower energy part of the XIS data is also useful for accurately constraining the thermal component.

Tycho's SNR was observed by Suzaku on 2006 June 26 through June 29 as part of the mission's Science Working Group program. The observation was carried out with the remnant's center placed at the center of the XIS CCD chip; the pointing coordinates were $(\alpha, \delta) = (00^{\text{h}}25^{\text{m}}20^{\text{s}}, 64^{\circ}08'18'')$ (equinox J2000.0). A nearby sky region, at coordinates $(\alpha, \delta) = (00^{\text{h}}36^{\text{m}}54^{\text{s}}, 64^{\circ}17'42'')$, $1^{\circ}27'$ offset from the SNR along the Galactic plane, was observed on 2006 June 29 in order to acquire background data. There are no known bright X-ray sources in the HXD field-of-view at the offset observation.

During these observations, 16 out of 64 silicon PIN diodes of the HXD were operated at a lower bias voltage (400 V) so as

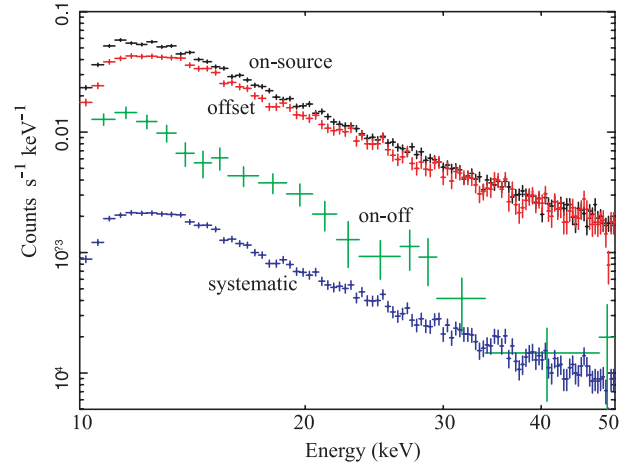


Fig. 1. On-source (black), off-source (red), and background-subtracted (green; on-off) spectra of Tycho's SNR, taken with HXD-PIN. The blue points show 5% of the background spectrum, as a measure of the systematic error associated with the background subtraction.

to avoid unexpected breakdown of the sensors. The other PIN diodes were operated at the nominal bias voltage of 500 V. The four XIS sensors, three front-illuminated CCD chips (XIS 0, XIS 2, and XIS 3) and a back-illuminated one (XIS 1), were operated in the standard mode.

2.2. HXD-PIN Data Reduction

In the analysis, we excluded data from the 16 PIN diodes operated at the lower bias voltage, because it is difficult at the present time to estimate their energy response and background accurately enough. We used cleaned events from the revision 1.2 data processing of the HXD data-reduction software. Data were excluded if acquired during potential high-background parts of the orbit (where the cutoff rigidity less than $8 \text{ GeV } c^{-1}$ or for 500 s after passage through the South Atlantic Anomaly), or when the target elevation was less than 5° above the horizon. The data selection was done using the XSELECT package of HEASOFT version 6.2. The net exposure after data selection was 92.0 ks and 45.8 ks for the Tycho and offset observations, respectively.

Although a generic non-X-ray background model is provided by the detector team, we used the offset observation data to estimate the total instrument and sky background of HXD-PIN. This is because we expect to achieve higher accuracy for HXD-PIN background subtraction when using the offset observation, which was carried out for a relatively long time just after the on-source observation, under nearly the same conditions for the non-X-ray background. We superposed orbital phases of the on-source and offset observations, and extracted the events from exactly the same orbital phase regions. The net on-source and off-source exposures used for making spectra were 74.5 ks and 37.3 ks, respectively.

Figure 1 shows the on-source, offset, and background-subtracted HXD-PIN spectra from 10 through 50 keV. We estimated the systematic error in the background spectra from Earth occultation data, which gives a measure of the non-X-ray background. We selected data with elevation from the Earth rim $\leq -5^{\circ}$ for both the on-source and offset observations,

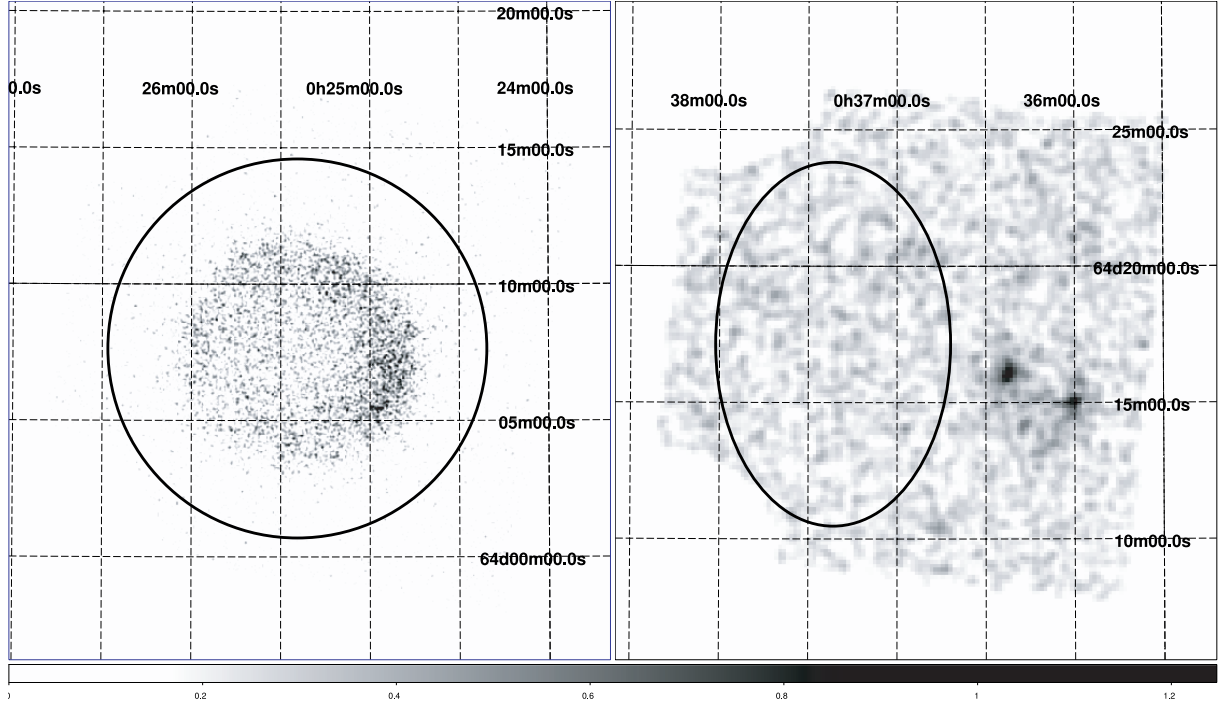


Fig. 2. (Left) X-ray image of Tycho's SNR taken by XIS 0 in 7–12 keV. The circle on the image indicates the region from which the on-source spectrum was derived. (Right) 5–12 keV image of the offset region on XIS 0. The ellipse indicates the region employed to produce the background spectrum.

retaining identical values for the other selection criteria. We compared the occultation events between the two observations, and found that they agree with each other to within 5% accuracy. In the following we adopt a value of 5% for the systematic error in the spectrum. To evaluate the background-subtraction accuracy in greater detail, we made a background-subtracted 12–30 keV light curve, and fitted it with a constant. The fit yielded a mean count rate and an associated 90% confidence-level error of $(5.66 \pm 0.31) \times 10^{-2} \text{ counts s}^{-1}$, with $\chi^2/\text{dof} = 1691/1547$. The light curve is thus consistent with a constant source (as expected for the SNR) thereby validating the background-subtraction technique. In figure 1, the level of the background systematic error (calculated as 5% of the offset spectrum) is shown. We thus securely detected the hard X-ray emission from Tycho's SNR up to 30 keV. The lowest end of the PIN spectrum extends to ~ 12 keV, as determined by thermal noise in the diodes (Kokubun et al. 2007).

For an extended source, like Tycho's SNR, an additional correction factor must be applied to the HXD-PIN effective area when trying to estimate the source flux. The remnant is about 8/2 in diameter, and the XIS pointed right at the center of the remnant ("XIS nominal position"). Although this correction factor should be included in the ancillary response files (ARFs) based on the specific morphology of the source, the current software tool `hxdarfgen` can calculate the response only for point sources. Therefore, to mimic a ring-like morphology (i.e., a rim-brightened structure as expected for Tycho's SNR), we assumed 8 point sources placed uniformly around a circle of 4/1 radius centered on the pointing direction. Then, we calculated an ARF for each of them, taking into account the 3/5 offset between the XIS and HXD optical axes. The final ARF

was obtained by just averaging the eight ARFs. To evaluate systematic errors associated with this ARF, we also generated a disk-like ARF with the same radius. The difference between the annular and disk-like ARFs was confirmed to be less than 1% in the 12–30 keV band.

2.3. XIS Data Reduction

For the XIS data reduction, we used cleaned events (revision 1.2) of the three front-illuminated CCDs (XIS 0, XIS 2 and XIS 3). The left panel of figure 2 shows the XIS image at energies between 7 and 12 keV. The region that we employed to extract the on-source spectrum is shown in the figure. The right panel of figure 2 shows an image of the offset observation, where an ellipse on the image indicates the region from which we extracted the background spectrum. Note that this region excluded an unknown diffuse, faint object visible in the XIS image of the offset observation. To evaluate the XIS background systematic error, we made another background file from the Lockman Hole observation (80 ks exposure). The difference between the offset and the Lockman Hole background spectra is 1% in the integrated 5–12 keV count rate, and the spectral shape is identical within statistical errors; we thus decided to use the offset background in the analysis.

ARF files describing the XIS effective area, combined with the X-ray mirror response, were generated by `xissimarfgen` (Ishisaki et al. 2007). To make the XIS ARF consistent with that of PIN, we generated the XIS ARFs assuming an annular source with a radius of 4/1. Since we are mainly interested in the hard X-ray emission, this assumption is justified by the XIS image above 7 keV, which reveals a clear ring-like source morphology.

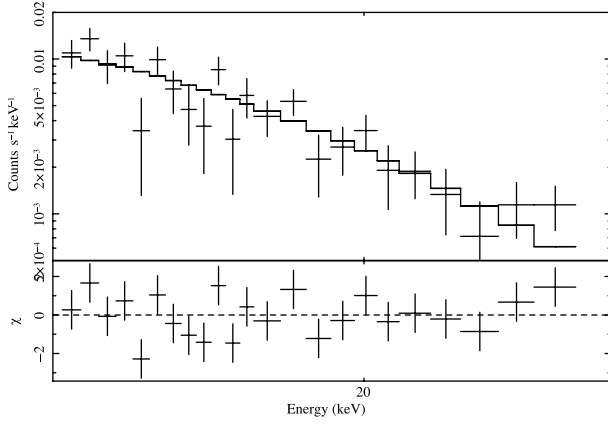


Fig. 3. PIN spectrum in 12–30 keV fitted with a power-law model and residuals.

3. Analysis and Results

3.1. Characterization of HXD-PIN Spectrum

Figure 3 shows the background-subtracted PIN spectrum of Tycho's SNR in the 12–30 keV band. We fitted the data successfully with a power-law model, and obtained a photon index of $\alpha_p = 2.83^{+0.56}_{-0.53}(\text{stat})^{+0.56}_{-0.03}(\text{syst})$ with $\chi^2/\text{dof} = 25.5/21$. The statistical error is shown at a confidence level of 90%, while the systematic error refers to a 5% uncertainty in estimating the background using the offset data. The residuals from the fit are also given in figure 3. If we assume the source of the emission to have an annular shape with a radius of $4'.1$, the 12–30 keV model flux is $(1.90^{+0.13}_{-0.128} {}^{+0.48}_{-0.30}) \times 10^{-11} \text{ erg cm}^{-2} \text{ s}^{-1}$. Alternatively, we fitted the PIN data with a thermal bremsstrahlung spectrum, and obtained a temperature of $kT = 12.4^{+8.2}_{-3.9} {}^{+0.9}_{-2.1} \text{ keV}$ with $\chi^2/\text{dof} = 27.1/21$. The 12–30 keV model flux is $(1.88^{+0.13}_{-0.89} {}^{+0.52}_{-0.62}) \times 10^{-11} \text{ erg cm}^{-2} \text{ s}^{-1}$. Thus, the two fits are both acceptable, although the power-law model is statistically somewhat favored.

3.2. Emission Lines above 4 keV

The atomic emission lines below 4 keV have been well studied by previous missions, including ASCA (Hwang & Gotthelf 1997), Chandra, and XMM-Newton (Decourchelle et al. 2001; Badenes et al. 2006). Here, we focus on the spectra above 4 keV, where Suzaku has a larger effective area and a lower background level than that of other missions. Figure 4a shows the XIS spectrum in the 4.1–8.5 keV energy range, where we can observe an intense Fe $K\alpha$ emission line. We fitted the spectrum with a composite model consisting of a power-law and a Gaussian. The best-fit parameters were $\alpha_p = 2.7$ and the Fe $K\alpha$ line center energy of 6.445 keV. The measured line center energy is in approximate agreement with that obtained with Tenma, $6.40 \pm 0.03 \text{ keV}$ (Tsunemi et al. 1986). This fit was not statistically acceptable ($\chi^2/\text{dof} = 447.6/180$), and there were clear residuals around 4.5, 5.5, 5.9, and 7.1 keV. The fit was significantly improved ($\chi^2/\text{dof} = 209.1/170$) by the addition of four more Gaussian lines. The best-fit model is also shown in figure 4a, and the residuals are given in figure 4b. Figure 4d shows a magnified view of the spectrum around the faint lines. The best-fit parameters of the

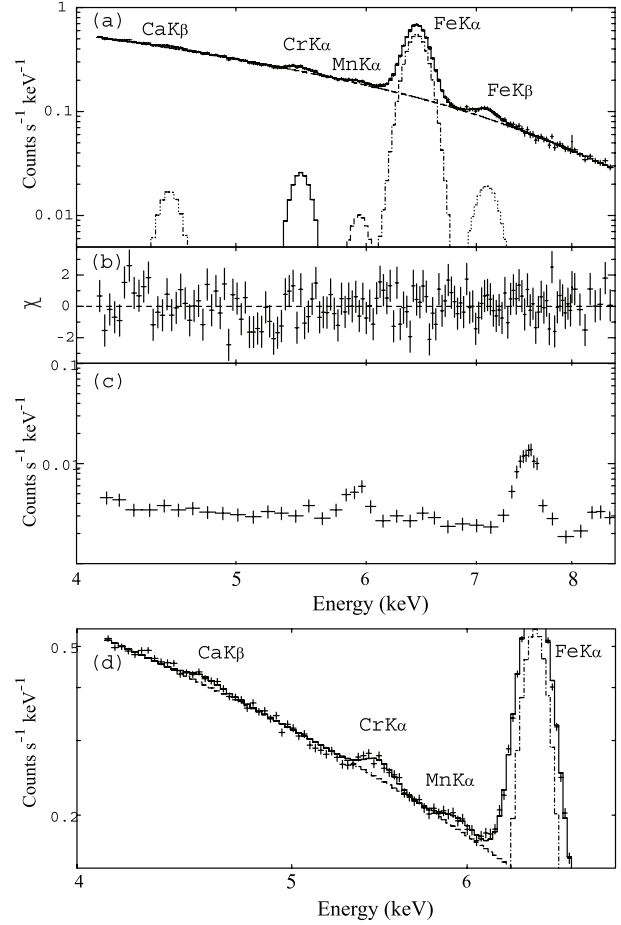


Fig. 4. (a) Summed spectrum of XIS0, 1, and 2 above 4 keV. A power-law and five Gaussian models are fitted to the data. (b) Residuals of the fitting. (c) Background spectrum. (d) Magnified spectrum in energies of 4–6.5 keV.

five Gaussians, including the central energy, flux, and equivalent width, are summarized in table 1. The background spectrum subtracted from the source spectrum is shown in figure 4c. The weak line at $\sim 5.90 \text{ keV}$ is leakage from the on-board ^{55}Fe calibration source, and only appears in sensor XIS 0. The line at $\sim 7.47 \text{ keV}$ is nickel fluorescence from the nearby structure of the XIS camera.

The lines at 4.56, 5.48, 5.95, and 7.11 keV have not been reported previously. Given the significant flux from He-like Ca $K\alpha$ (Badenes et al. 2006), the simplest explanation for the 4.56 keV line is He-like Ca $K\beta$. (Furthermore, the expected He-like Ca $K\beta$ energy centroid of 4.58 keV is consistent with our line measurements.) The next two lines, 5.48 and 5.95 keV, are probably $K\alpha$ lines from elements near Fe on the periodic table. They exhibit slightly higher energies than the $K\alpha$ lines of neutral Cr and Mn, which are centered at 5.41 and 5.90 keV, respectively. To evaluate their nature, we plotted their energy, E_i , as a function of the atomic number, Z_i , and fitted to Moseley's law (Moseley 1913, 1914),

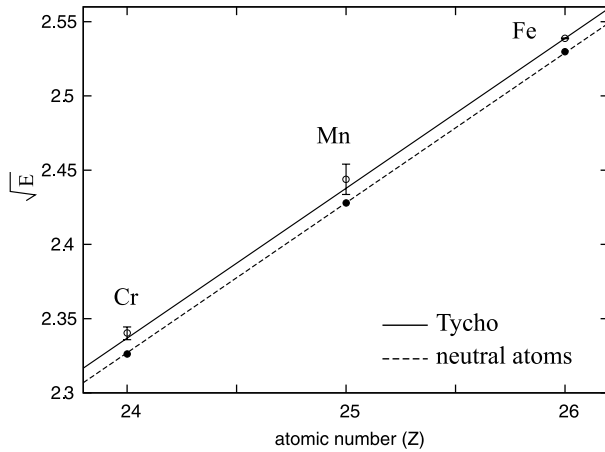
$$E_i = a (Z_i - b)^2. \quad (1)$$

It is known that the normalization factor is $a = 3/4 \text{ Ry} = 1.02 \times 10^{-2} \text{ keV}$ with Rydberg energy (Ry) and the screening factor

Table 1. Emission lines above 4 keV.*

Line	Central energy [†] (keV)	Width (eV)	Flux [‡] ($\times 10^{-5}$ photons cm $^{-2}$ s $^{-1}$)	Equivalent width (eV)
Ca K β	4.56 (4.52, 4.60)	= Fe K α	1.68 (1.03, 2.16)	9.7 (1.8, 17.5)
Cr K α	5.48 (5.46, 5.50)	= Fe K α	2.45 (2.03, 2.93)	23.8 (13.0, 32.3)
Mn K α	5.95 (5.90, 6.00)	= Fe K α	1.13 (0.68, 1.51)	13.7 (2.7, 27.2)
Fe K α	6.445 (6.444, 6.446)	52.7 (50.0, 54.5)	69.1 (68.2, 69.7)	$1.04 (1.02, 1.07) \times 10^3$
Fe K β	7.11 (7.09, 7.13)	82.4 (42.1, 122.4)	3.55 (2.87, 4.17)	70.5 (47.1, 95.2)
Ni K α	7.51 [§]	= Fe K α	0.82	25.1

* Denotes 90% confidence-level error.

[†] Continuum component is a power-law with a photon index $\alpha_p = 2.76 \pm 0.02$.[‡] Assuming annulus source with a radius of 4'.1.[§] Estimated from the other lines (see text).^{||} 90% confidence-level upper limit.**Fig. 5.** Measured line energies composed with a prediction of the Moseley's law. The energies of K α lines of neutral atoms from Cr to Fe are plotted on the same figure.

is $b \sim 1$ for K α lines of neutral atoms. Figure 5 shows the line energies determined in this analysis and K α lines from neutral atoms of $Z = 24$ –26, together with results obtained by fitting equation (1). In the fits, we fixed a to that of neutral species, and allowed b to vary. The best-fit value obtained was $b = 0.862 \pm 0.002$, and the new K α lines fell on Moseley's law within the uncertainties. We thus conclude that the lines are from similarly ionized states of Cr, Mn, and Fe. We note that there is a weak contamination line at 5.90 keV (figure 4c), but this appears only in XIS 0, while the 5.95 keV line was detected in all XIS instruments.

If we extrapolate our best fit to Moseley's law, we can estimate the centroid energy of the Co ($Z = 27$) and Ni ($Z = 28$) K α lines to be 6.97 and 7.51 keV. Neither value matches the line centroid of the 7.11 keV feature, from which we conclude that the line at 7.11 keV is probably the Fe K β blend. The low central energies of both the Fe K α and Fe K β line blends indicate that the emitting iron is in an extremely low ionization condition. The central energies of K α and K β are consistent with those of Fe XV or XVI, as calculated by Mendoza et al. (2004). Assuming these ionization states, the Fe K β to K α flux ratio, $f(\text{K}\beta)/f(\text{K}\alpha) = 0.04 \pm 0.01$, is consistent

with Mendoza et al. (2004), who calculated this flux ratio for K-vacancy configurations of iron atoms.

Although there was no significant excess emission at energies corresponding to the Ni K α in the XIS spectrum (figure 4a), we estimated the upper limit of the Ni K α flux by adding a Gaussian with its centroid energy fixed at 7.51 keV. The fits yielded a 90%-confidence upper limit flux and an equivalent width of 8.15×10^{-6} photons cm $^{-2}$ s $^{-1}$ and 25.1 eV, respectively (table 1).

3.3. PIN and XIS Joint Fitting with Conventional Models

To characterize the continuum spectrum of Tycho's SNR, we fitted the XIS spectra above 5 keV simultaneously with the 12–30 keV PIN spectrum. Since the lines from Cr and Mn introduced above are not taken into account in current nonequilibrium ionization models, we fitted the data with conventional (power-law or thermal bremsstrahlung) models plus four Gaussians. In the fitting, the low-energy absorption was fixed to $N_H = 0.7 \times 10^{22}$ cm $^{-2}$, as obtained by Cassam-Chenaï et al. (2007), while the other parameters were left to be free. As calibrated by Kokubun et al. (2007) using the Crab Nebula, the model normalization to fit the PIN data was set 13% higher than that of the XIS data.

First, we fitted the spectra with a thermal bremsstrahlung model plus Gaussians. Figure 6a shows the fit result and residuals. The best-fit parameter value was $kT = 5.14^{+0.14}_{-0.12}$ keV. The fit yielded a relatively large $\chi^2/\text{dof} = 253.8/175$, and there was clear excess above 10 keV. In an attempt to reduce the χ^2 value, we next added another bremsstrahlung component to the model. Figure 6b shows the best-fit spectrum and residuals. The best-fit value was $kT_{\text{low}} = 3.48^{+0.59}_{-1.19}$ keV and $kT_{\text{high}} = 22.9^{+12.9}_{-12.9}$ keV with $\chi^2/\text{dof} = 185.9/173$. These values are similar to those from the Ginga spectral analysis, in which the temperatures were $kT_{\text{low}} = 2.71$ keV and $kT_{\text{high}} = 11.6$ keV (Fink et al. 1994). Although the two thermal bremsstrahlung model is statistically acceptable, the temperature of the hotter component, kT_{high} , is probably too high to reflect thermal emission from the remnant. At face value, it suggests a shock speed of a few thousand km s $^{-1}$, but recent work indicates that very little electron heating occurs in such high-speed shocks, since the level of electron heating is observed to decrease strongly with increasing shock speed (Rakowski et al. 2003).

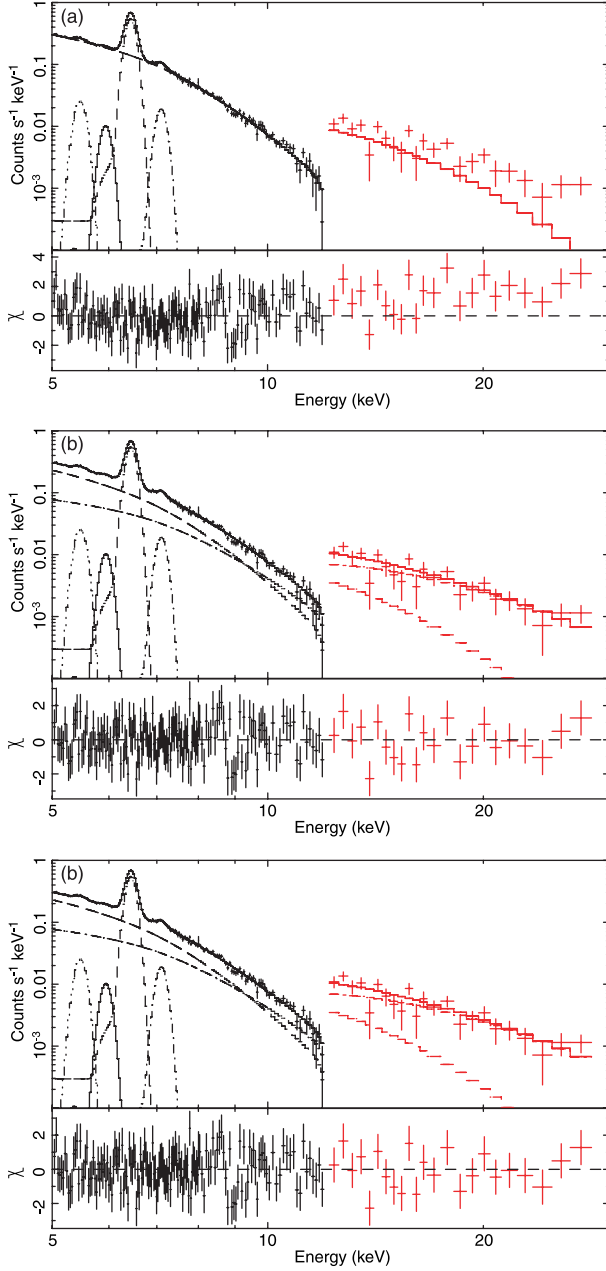


Fig. 6. XIS and PIN spectra fitted with (a) a thermal bremsstrahlung model, (b) two thermal bremsstrahlung models, and (c) a thermal bremsstrahlung and a power-law models. Fit residuals are also plotted in the figures. The emission lines of Cr, Mn, and Fe are represented in the fit by Gaussian models.

The actual shock velocity, corresponding to a 22.9 keV electron temperature in Tycho's SNR, would have to be so high as to be unreasonable. Moreover, the upper limit on the higher temperature component is not constrained, as shown in figure 7. This strongly suggests that the harder spectral component is of nonthermal origin, rather than thermal.

In our ultimate model, we fitted the spectrum with a thermal bremsstrahlung component and a power-law plus Gaussians. Figure 6c shows the model spectra and residuals. The best-fit parameters were $kT = 4.71^{+0.66}_{-1.02}$ keV and $\alpha_p = 2.69^{+0.23}_{-1.27}$ with $\chi^2/\text{dof} = 185.9/173$. The power-law model flux at 1 keV

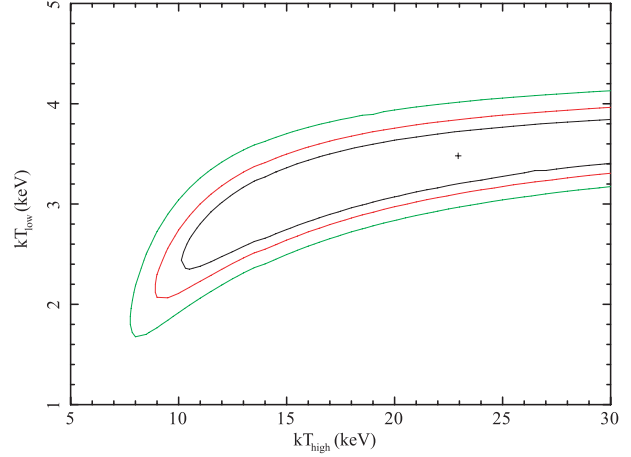


Fig. 7. 68%, 90%, and 99% significance contours of the two thermal bremsstrahlung fit.

is 7.3×10^{-2} photons $\text{cm}^{-2} \text{s}^{-1} \text{keV}^{-1}$, which corresponds to a 10–20 keV band model flux of $1.3 \times 10^{-11} \text{erg cm}^{-2} \text{s}^{-1}$. From these results, we conclude that the power-law component with $\alpha_p = 2.69$ extends beyond 20 keV, which is the uppermost energy of the Ginga observations (Fink et al. 1994), up to at least 30 keV.

4. Discussion

4.1. Origin of the Hard X-Ray Emission

We have found that the hard power-law tail of Tycho's SNR's spectrum extends up to energies of at least 30 keV with a photon index of ~ 2.69 . The photon index is consistent with those observed by Chandra from the rim regions of the SNR in 0.5–10 keV low energy band (Hwang et al. 2002; Warren et al. 2005; Cassam-Chenaï et al. 2007). We further verified that the overall normalization of the power-law component in the integrated Chandra spectrum is consistent with the power-law normalization we found here. Thus, we conclude that the featureless power-law spectra observed in the Chandra energy region naturally extends to the Suzaku HXD-PIN energy region up to at least 30 keV. It is natural to interpret that the emission comes from synchrotron radiation.

4.2. Roll-Off Frequency of the Synchrotron Spectrum

The steep slope of the power-law model ($\alpha_p = 2.69$) indicates that the synchrotron emission we observed in the Suzaku energy region is above the roll-off frequency of the spectrum extrapolated from the radio regime. Assuming a power-law electron number spectrum, $N(E)$, with an exponential cutoff energy of

$$N(E) = K E^{-s} \exp(-E/E_{\text{max}}), \quad (2)$$

where s is an electron power-law index and E_{max} is the maximum electron energy, we can estimate the synchrotron roll-off frequency. Using the electron spectrum, we can simply derive the photon spectrum from radio to X-ray by superposing the single-particle synchrotron emissivities while assuming a constant magnetic field. This spectral model is implemented in the XSPEC package as an `srcut` model

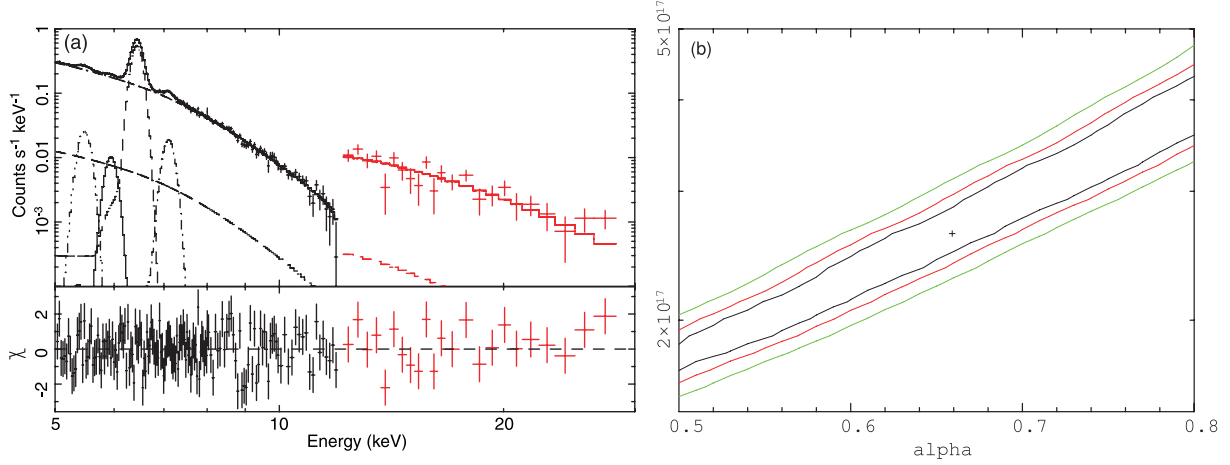


Fig. 8. (a) XIS and PIN spectra fitted with a thermal bremsstrahlung, an srcut model, and Gaussian lines. (b) 68%, 90%, and 99% significance contours of the fit.

(Reynolds & Keohane 1999).

We fitted the XIS and PIN spectra with a thermal bremsstrahlung, an srcut model, and Gaussian lines corresponding to Cr, Mn, Fe $K\alpha$, and Fe $K\beta$. In the fits, we fixed the Gaussian parameters and the temperature to $kT = 4.71$ keV, which are derived in subsection 3.3, while the parameters of the srcut model were left free. As shown in figure 8a, the fit was successful with $\chi^2/\text{dof} = 187.4/173$. Although the parameters were rather unconstrained, as shown in figure 8b, the obtained radio spectral index, $\alpha = 0.66$, is in a good agreement with the measured value of $\alpha = 0.65$ (Kotthes et al. 2006), and the implied radio flux density at 1 GHz, 45 Jy, is not far from the actual measurement (60 Jy: Kotthes et al. 2006). Therefore, our srcut fit appears to be physically appropriate. Then, adopting $\alpha = 0.65$, we obtained a roll-off frequency of $\nu_{\text{rolloff}} = 2.6 \times 10^{17} \text{ Hz} = 1.1 \text{ keV}$, which is slightly higher than that derived by Chandra ($\nu_{\text{rolloff}} = 7.3 \times 10^{16} \text{ Hz} = 0.3 \text{ keV}$; Cassam-Chenaï et al. 2007).

The roll-off frequency ν_{rolloff} is related to the maximum electron energy, E_{max} , as

$$\nu_{\text{rolloff}} = 5 \times 10^{15} \left(\frac{B}{10 \mu\text{G}} \right) \left(\frac{E_{\text{max}}}{10 \text{ TeV}} \right)^2, \quad (3)$$

where B represents the magnetic field strength. Warren et al. (2005) presented a summary of magnetic field values, and gave values in the range of 100 to 400 μG . Then, equation (3) yields $E_{\text{max}} = 23 \text{ TeV}$ with 100 μG , or 12 TeV for 400 μG . Even if we use the fiducial magnetic field in our Galaxy, 10 μG , the maximum electron energy is only 72 TeV.

These maximum electron energies are two to three orders of magnitudes below the break energy (“knee”) of the cosmic-ray spectrum around 1000 TeV. Reynolds and Keohane (1999) pointed out that the E_{max} values of all Galactic supernova remnants that they studied with ASCA data were well below the knee energy. To evaluate the role of radiative cooling on the electron energy spectrum, we approximate the synchrotron radiation loss timescale, τ_{loss} , as

$$\tau_{\text{loss}}(\text{yr}) = 1.2 \times 10^4 \left(\frac{B}{10 \mu\text{G}} \right)^{-2} \left(\frac{E_{\text{max}}}{10 \text{ TeV}} \right)^{-1}. \quad (4)$$

With our estimate of $E_{\text{max}} = 23 \text{ TeV}$ and magnetic field strength of 100 μG , τ_{loss} is 52 yr. Since the time scale is smaller than the age of Tycho’s SNR (435 yr), the electron spectrum should suffer strongly from synchrotron cooling. This has been directly detected in the Chandra data of Tycho’s SNR as spectral steepening in the nonthermal emission across the featureless, thin filaments at the rim (Cassam-Chenaï et al. 2007).

4.3. Abundance of Cr, Mn, and Fe

We discovered He-like Ca $K\beta$, and underionized states of Cr $K\alpha$, Mn $K\alpha$, and Fe $K\beta$ lines from Tycho’s SNR for the first time. The ionization degrees of Cr and Mn were estimated to be similar to that of Fe $K\alpha$ (Ne-like or thereabouts). To convert the measured line fluxes or equivalent widths (table 1) into elemental abundances, a detailed emissivity calculation is needed. However, this is beyond the scope of the present paper, since the current models that calculate X-ray emission under the nonequilibrium ionization conditions do not include the species Cr and Mn.

The relative abundances of trace elements, such as Cr and Mn, are sensitive to the Type Ia supernova explosion mechanism (Iwamoto et al. 1999), and therefore should provide an important diagnostic for these explosions. However, the compositionally stratified nature of the supernova ejecta coupled with the inward progression of the reverse shock, means that great care needs to be taken when comparing observed line fluxes and yields from model calculations. In particular, a good fraction of the Fe produced in the explosion that Tycho Brahe observed in 1572 still sits unshocked and cold in the center of the remnant (Badenes et al. 2006). To fully interpret the results presented here will require accounting for the ejecta structure and its subsequent hydrodynamical evolution to the remnant phase. Cr and Mn $K\alpha$ lines were detected previously only from W 49B (in which the X-ray emitting gas is nearly in collisional ionization equilibrium), where the abundances were found to be consistent with solar values (Hwang et al. 2000; Miceli et al. 2006). Detailed emissivity calculations for trace species in nonequilibrium hot plasmas are strongly encouraged to open this new method for supernova nucleosynthesis diagnostics.

5. Conclusions

We report the first observation of Tycho's SNR by the Suzaku satellite. We focused on the X-ray spectra above 4 keV and obtained the following results:

1. X-ray emission was securely detected up to at least 30 keV with a power-law index of 2.69. When combined with the Chandra spectra at Tycho's rim regions, it is natural to interpret that the emission comes from synchrotron radiation.
2. We discovered four emission lines. The line central

energies are 4.56, 5.48, 5.95, and 7.11 keV, corresponding to He-like Ca $K\beta$, and low ionized Cr $K\alpha$, Mn $K\alpha$, and Fe $K\beta$ blends, respectively. When combined with detailed emissivity calculations and evolutionary models for the remnant X-ray emission, these new lines should provide important new diagnostics to constrain the nature of thermonuclear supernovae.

The authors thank all of the Suzaku Science Working Group members for their extensive discussions. JPH acknowledges support from NASA grant NNG05GP87G.

References

- Ammosov, A. E., Ksenofontov, L. T., Nikolaev, V. S., & Petukhov, S. I. 1994, *Astr. Lett.*, 20, 157
- Badenes, C., Borkowski, K. J., Hughes, J. P., Hwang, U., & Bravo, E. 2006, *ApJ*, 645, 1373
- Bamba, A., Yamazaki, R., Yoshida, T., Terasawa, T., & Koyama, K. 2005, *ApJ*, 621, 793
- Cassam-Chenaï, G., Hughes, J. P., Ballet, J., & Decourchelle, A. 2007, *ApJ*, 665, 315
- Decourchelle, A., et al. 2001, *A&A*, 365, L218
- Fink, H. H., Asaoka, I., Brinkmann, W., Kawai, N., & Koyama, K. 1994, *A&A*, 283, 635
- Hwang, U., Decourchelle, A., Holt, S. S., & Petre, R. 2002, *ApJ*, 581, 1101
- Hwang, U., & Gotthelf, E. V. 1997, *ApJ*, 475, 665
- Hwang, U., Petre, R., & Hughes, J. P. 2000, *ApJ*, 532, 970
- Ishisaki, Y., et al. 2007, *PASJ*, 59, S113
- Iwamoto, K., Brachwitz, F., Nomoto, K., Kishimoto, N., Umeda, H., Hix, W. R., & Thielemann, F.-K. 1999, *ApJS*, 125, 439
- Kokubun, M., et al. 2007, *PASJ*, 59, S53
- Kothes, R., Fedotov, K., Foster, T. J., & Uyaniker, B. 2006, *A&A*, 457, 1081
- Koyama, K., et al. 2007, *PASJ*, 59, S23
- Koyama, K., Petre, R., Gotthelf, E. V., Hwang, U., Matsuura, M., Ozaki, M., & Holt, S. S. 1995, *Nature*, 378, 255
- Mendoza, C., Kallman, T. R., Bautista, M. A., & Palmeri, P. 2004, *A&A*, 414, 377
- Miceli, M., Decourchelle, A., Ballet, J., Bocchino, F., Hughes, J. P., Hwang, U., & Petre, R. 2006, *A&A*, 453, 567
- Mitsuda, K., et al. 2007, *PASJ*, 59, S1
- Moseley, H. G. J. 1913, *Phil. Mag.*, 1024
- Moseley, H. G. J. 1914, *Phil. Mag.*, 703
- Petre, R., Allen, G. E., & Hwang, U. 1999, *Astron. Nachr.*, 320, 199
- Pravdo, S. H., & Smith, B. W. 1979, *ApJ*, 234, L195
- Rakowski, C. E., Ghavamian, P., & Hughes, J. P. 2003, *ApJ*, 590, 846
- Reynolds, S. P., & Keohane, J. W. 1999, *ApJ*, 525, 368
- Serlemitsos, P. J., et al. 2007, *PASJ*, 59, S9
- Takahashi, T., et al. 2007, *PASJ*, 59, S35
- Tsunemi, H., Yamashita, K., Masai, K., Hayakawa, S., & Koyama, K. 1986, *ApJ*, 306, 248
- Warren, J. S., et al. 2005, *ApJ*, 634, 376